

# Revision 1

## Water in the Crystal Structure of CaSiO<sub>3</sub> Perovskite

Sang-Heon Shim<sup>1</sup>, Andrew Chizmeshya<sup>2</sup>, and Kurt Leinenweber<sup>3</sup>

<sup>1</sup> School of Earth and Space Exploration, Arizona State University, Tempe, Arizona 85287, U.S.A.

<sup>2</sup> School of Molecular Sciences, Arizona State University, Tempe, Arizona 85287, U.S.A.

<sup>3</sup> Eyring Materials Center, Arizona State University, Tempe, Arizona 85287, U.S.A.

### Abstract

While the water storage capacities of the upper 700-km depths of the mantle have been constrained by high-pressure experiments and diamond inclusion studies, the storage capacity of the lower mantle remains controversial. A recent high-pressure experimental study on CaSiO<sub>3</sub> perovskite, which is the third most abundant mineral in the lower mantle, reported possible storage of H<sub>2</sub>O up to a few weight percent. However, the substitution mechanism for H in the phase remains unknown. We have conducted a series of density functional theory calculations under static-lattice conditions and high pressures to elucidate hydration mechanisms at the atomic scale. All of the possible dodecahedral (Ca<sup>2+</sup> → 2H<sup>+</sup>) and octahedral (Si<sup>4+</sup> → 4H<sup>+</sup>) substitution configurations for a tetragonal perovskite lattice have very small energy differences, suggesting coexistence of multiples of H configurations in CaSiO<sub>3</sub> perovskite at mantle pressures and temperatures. The dodecahedral substitutions decrease the bulk modulus, resulting in smaller unit-cell volume of hydrous CaSiO<sub>3</sub> perovskite under pressure, consistent with the experimental observations. Although the octahedral substitutions also decrease the bulk modulus, they increase the unit-cell volume at 1 bar. The H atoms substituted in the dodecahedral sites develop much less hydrogen bonding with O atoms, leading to a large distortion in the neighboring SiO<sub>6</sub> octahedra. Such distortion may be responsible for the non-cubic peak splittings observed in experiments on hydrous CaSiO<sub>3</sub> perovskite. Our calculated infrared spectra suggest that the observed broad OH modes in CaSiO<sub>3</sub> perovskite can result from the existence of multiples of H configurations in the phase. Combined with the recent experimental results, our study suggests that CaSiO<sub>3</sub> can be an important mineral phase to consider for the H<sub>2</sub>O storage in the lower

30 mantle.

31 **Keywords:** CaSiO<sub>3</sub> perovskite; water; mantle; first-principles calculation

32

## 33 **Introduction**

34 Global cycles involving volatile elements, such as hydrogen, are important for a range of process  
35 in Earth and planetary systems, including interior-atmosphere interaction, mantle mixing and  
36 convection, and surface tectonics (Bolfan-Casanova, 2005; Hirschmann, 2006; Ohtani et al.,  
37 2016). Laboratory studies have shown that some nominally anhydrous minerals (NAMs) in the  
38 mantle transition zone can contain a large amount of H<sub>2</sub>O in the crystal structure (Kohlstedt et  
39 al., 1996; Smyth, 1994; Bell and Rossman, 1992), which has been recently supported by  
40 diamond inclusion studies (Pearson et al., 2014).

41 However, the H<sub>2</sub>O storage capacities of the major nominally anhydrous mineral phases in the  
42 lower mantle have been controversial. Earlier studies proposed a possible large storage for  
43 bridgmanite (Murakami et al., 2002; Litasov et al., 2003). Later, it was suggested that existence  
44 of small hydrous inclusions can bias the earlier results and that the H<sub>2</sub>O storage capacity of  
45 bridgmanite is very low compared with the nominally anhydrous mineral phases in the mantle  
46 transition zone (Bolfan-Casanova, 2005; Panero et al., 2015). However, a more recent study  
47 reported a large amount of H<sub>2</sub>O stored in bridgmanite synthesized from melt (Fu et al., 2019).  
48 Therefore, the H<sub>2</sub>O storage capacity of bridgmanite remains uncertain. It appears that  
49 ferropericlase can contain only a very small amount of H<sub>2</sub>O (Bolfan-Casanova et al., 2003).

50 CaSiO<sub>3</sub> perovskite is the third most abundant phase in the pyrolitic lower mantle composition  
51 (Kesson et al., 1998; Lee et al., 2004). It is one of the main mineral phases in subducting oceanic  
52 crust materials (Hirose et al., 2005; Ricolleau et al., 2010; Grocholski et al., 2012). Inclusions in  
53 diamond crystals from the deep mantle support the existence of CaSiO<sub>3</sub> perovskite in the lower  
54 mantle (Smith et al., 2018; Nestola et al., 2018). The importance of the crystal structure and  
55 elastic properties of CaSiO<sub>3</sub> perovskite has been also highlighted for the topmost lower mantle  
56 and the core-mantle boundary region in some recent studies (Thomson et al., 2019; Gréaux et al.,  
57 2019). Astrophysical studies have shown that some stars may produce a larger amount of Ca

58 (Hinkel and Unterborn, 2018). Earth-like exoplanets around those stars may therefore contain a  
59 larger amount of  $\text{CaSiO}_3$  perovskite in their lower mantle. Accordingly, it is important to  
60 measure possible storage of  $\text{H}_2\text{O}$  and its impact for the equation of state for understanding the  
61 geophysics and geochemistry of those planets. Although some studies have suggested possible  
62  $\text{H}_2\text{O}$  storage in this mineral phase (Murakami et al., 2002; Németh et al., 2017; Chen et al.,  
63 2020), it has been difficult to characterize the amount of  $\text{H}_2\text{O}$  possibly stored in the mineral. The  
64 main reason has been that  $\text{CaSiO}_3$  perovskite is not quenchable to 1 bar, which makes it difficult  
65 to conduct H quantification (such as secondary ion mass spectrometry, SIMS) as the technique  
66 requires the recovery of high-pressure samples to 1 bar.

67 In the most recent experimental study, Chen et al. (2020) proposed a percent level solubility of  
68  $\text{H}_2\text{O}$  in the crystal structure of  $\text{CaSiO}_3$  perovskite. Hampered by the amorphization and the  
69 limitations in characterization techniques, the quantity and substitution mechanism remain  
70 unclear. Nevertheless, they observed a number of important changes in  $\text{CaSiO}_3$  perovskite upon  
71 hydration at high pressures. In particular, (1) H substitution is found to decrease the unit-cell  
72 volume of  $\text{CaSiO}_3$  perovskite and (2) tetragonal distortion persists to mantle-related temperatures  
73 for hydrous  $\text{CaSiO}_3$  perovskite. The latter behavior is in contrast with observations for anhydrous  
74  $\text{CaSiO}_3$  perovskite in that stability of cubic structure known at mantle-related temperatures for  
75 the anhydrous case (Kurashina et al., 2004a; Chen et al., 2018). Chen et al. (2020) also found the  
76 formation of  $\delta\text{-AlOOH}$  in an experiment where Al-bearing  $\text{CaSiO}_3$  was heated in an  $\text{H}_2\text{O}$   
77 medium. The result indicates that  $\text{H}_2\text{O}$  changes the partition behavior of Al such that Al does not  
78 dissolve in  $\text{CaSiO}_3$  in a presence of  $\text{H}_2\text{O}$  unlike anhydrous system where up to 10 wt% solubility  
79 of Al has been documented (Gréaux et al., 2011). The observation also suggests that  $\text{Si}^{4+} \rightarrow \text{Al}^{3+}$   
80 +  $\text{H}^+$  mechanism (Pawley et al., 1993; Navrotsky, 1999; Litasov et al., 2003, 2007) would not be  
81 a major factor for the storage of  $\text{H}_2\text{O}$  in the case of  $\text{CaSiO}_3$  perovskite and direct substitution of  
82 Ca ( $\text{Ca}^{2+} \rightarrow 2\text{H}^+$ ) (Beran et al., 1996) and Si ( $\text{Si}^{4+} \rightarrow 4\text{H}^+$ ) (Spektor et al., 2011) should be  
83 considered. However, because of the experimental difficulties, most notably the inability of X-  
84 ray diffraction to directly resolve H atom locations, these experiments could not confirm the H  
85 substitution hypothesis in  $\text{CaSiO}_3$  perovskite. Density functional theory (DFT) based simulation  
86 provides an important tool to examine such proposed substitution mechanisms. The calculation  
87 can also address if  $\text{H}_2\text{O}$  substitution can lead to the observed changes in unit-cell parameters and  
88 symmetry of  $\text{CaSiO}_3$  perovskite in Chen et al. (2020). While DFT methods have been used for

89 studying the physical properties and crystal structure of CaSiO<sub>3</sub> perovskite (Chizmeshya et al.,  
90 1996; Akber-Knutson et al., 2002; Magyari-Köpe et al., 2002; Jung and Oganov, 2005; Caracas  
91 et al., 2005; Stixrude et al., 2007; Kawai and Tsuchiya, 2015; Thomson et al., 2019), to our  
92 knowledge, there is no DFT study examining the possible substitution of H<sub>2</sub>O in CaSiO<sub>3</sub>  
93 perovskite. MgSiO<sub>3</sub> perovskite (bridgmanite) has a similar structure with a lower symmetry  
94 (orthorhombic). Hernández et al. (2013) has conducted DFT calculation for H substitution in  
95 bridgmanite. However, they focused primarily on the partitioning of H among bridgmanite,  
96 ringwoodite, and periclase, and only one configuration was used to represent each of the  
97 dodecahedral and the octahedral substitutions.

98 In this study, we explore the energetics and impact of Ca<sup>2+</sup> → 2H<sup>+</sup> and Si<sup>4+</sup> → 4H<sup>+</sup> substitutions  
99 on the energetics and the crystal structure of CaSiO<sub>3</sub> perovskite. The focus of our study is to  
100 examine if the experimentally observed changes in unit-cell parameters and symmetry of CaSiO<sub>3</sub>  
101 perovskite can be explained by these substitution mechanisms. In addition, we calculated  
102 infrared spectra of a few chosen H configurations and compared them with the reported IR  
103 spectra for the OH vibration in CaSiO<sub>3</sub> perovskite.

104

## 105 **Method**

### 106 **Density functional theory calculation**

107 We conducted the density functional theory (DFT) calculations using both the GPAW code  
108 (Enkovaara et al., 2010) and the VASP code (Kresse and Furthmüller, 1996) with generalized  
109 gradient approximations (GGA) for the exchange correlation potentials. For GGA we used PBE  
110 exchange-correlation functional (Perdew et al., 1996). For the projected augmented wave (PAW)  
111 (Blöchl, 1994) method adopted here a plane-wave cutoff of 1000 eV was sufficient to converge  
112 the unit-cell electronic energy to the meV level, and reduce the residual atomic forces to 0.03 eV/  
113 Å. We tested the calculations for a higher cutoff energy (1200 eV) and a lower residual atomic  
114 forces (0.01 eV/Å). We found negligible changes in these tests, such as less than 0.0006 Å  
115 changes in unit-cell parameters, 0.01 Å changes in the bond distances, and 0.02° changes in the  
116 bond angles. The outcomes obtained from GPAW and VASP were found to be essentially

117 indistinguishable.

118 We adapted the tetragonal structure reported in Chen et al. (2018) for the anhydrous CaSiO<sub>3</sub>  
119 perovskite model. The space group of the initial model structure is *I4/mcm* with approximately 7-  
120 degree anti-phase rotations of the octahedra in the framework with rotation vectors along one  
121 primary axis – the *a0a0c*– rotation group in the Glazer notation (Glazer, 1972). The *c*-axis is  
122 doubled compared to the perovskite aristotype. We constructed a 2×2×1 supercell of the  
123 tetragonal cell and then remove all the symmetry constraints for calculations of a *P1* cell.  
124 Therefore, our ‘Anhy’ model cell contains a total of 80 atoms (or 16CaSiO<sub>3</sub>). We used  
125 Monkhorst-Pack sampling (Monkhorst and Pack, 1976): a total of 96 points (4×4×6). A greater  
126 sampling for (6×6×8) does not lead to any significant difference in the crystal structure results.  
127 We conducted simultaneous optimization for the atomic positions and lattice constants using the  
128 Broyden-Fletcher-Goldfarb-Shanno algorithm (BFGS) in the Atomic Simulation Environment  
129 (Larsen et al., 2017) in the static lattice approximation (e.g., no zero-point motion or thermal  
130 corrections). The calculations were conducted at seven different pressures: 0, 20, 40, 60, 80, 100,  
131 and 120 GPa.

## 132 **Hydrogen substitution models**

133 For storage of H<sub>2</sub>O in CaSiO<sub>3</sub> perovskite, we consider two possible substitution mechanisms:  
134 dodecahedral Ca substitution (hereafter CaH models),



136 and octahedral Si substitution (hereafter SiH models),



138 The Ca and Si substitutions result in 0.99 and 1.96 wt% H<sub>2</sub>O in the crystal structure of CaSiO<sub>3</sub>  
139 supercell we consider in this study, respectively. We also examined two Ca vacancies for two  
140 CaH models (see below). The content of H<sub>2</sub>O in this case is 2.02 wt%.

141 In the CaH models, two H atoms bond with two O atoms out of 12O atoms in a dodecahedral site  
142 (Fig. 1). From the symmetry of the Ca-O dodecahedron in the tetragonal perovskite structure  
143 expected for anhydrous CaSiO<sub>3</sub>, we identified three groups of O atoms (“S”, “E”, and “L”). For  
144 each of the “S” and “L” cases, the four O atoms form a tetrahedral motif as depicted by different

145 colors in Fig. 1. The “S” and “L” oxygen atoms are distinguished by their distances from the  
146 dodecahedral center where a Ca atom exists. Two of those four O atoms (S or L) can form  
147 bonding with two H atoms, resulting in two different cases: H atoms bond with (1) two O atoms  
148 at the same  $z$  locations (such as S1-S2, S3-S4, L5-L6, and L7-L8 in the figure; CaH-SS or CaH-  
149 LL in Tab. 1), and (2) two O atoms at the different  $z$  locations (such as S1-S3, S1-S4, L5-L7, and  
150 L5-L8; CaH-SS' or CaH-LL').

151 The O atoms in the third group have intermediate distances from the center of the dodecahedron  
152 (E's in Fig. 1). They form a square. Considering degeneracy, there are two cases to consider: H  
153 atoms bond with (1) two O atoms at the opposite corners (such as E9-E10; CaH-EE<sub>2</sub> where 2  
154 means second neighbor) and (2) two O atoms at the same edge (such as E9-E11; CaH-EE where  
155 absence of any number at the end means next neighbor).

156 We also consider cases where two H atoms bond with O atoms in different groups (Tab. 1). For  
157 example, CaH-SE<sub>2</sub> has H atoms bonded to O(S) and O(E) at the second neighbor, such as S1-E9.  
158 CaH-SL'3 has H atoms bonded to O(S) and O(L) in two layers separated by O(E) atoms and they  
159 are third neighbors, such as S1-L7 in Fig. 1. For some cases which will be discussed later in this  
160 paper, “S” and “L” O atoms become indistinguishable after optimization. We identified 10  
161 energetically distinct structures for the CaH model group as shown in Tab. 1.

162 For the octahedral site hydration models (Eq. 2), we have identified four possible configurations  
163 for H substitution (Tab. 1). Because oxygen atoms at both S and L in an octahedron are bonded  
164 with neighboring Ca atoms at both distances, these oxygen atoms are no longer distinct with each  
165 other and therefore SiH-SSLE is, for example, equivalent to SiH-LLSE. However, SLEE and  
166 SSEE are distinct configurations. The oxygen atoms at L and S are located in the equatorial  
167 plane of an octahedron as shown in Fig. 2. Two O(S)'s are located diagonal positions in the  
168 plane. Therefore, in SLEE, H atoms bond to two neighboring oxygen atoms in the plane, while in  
169 SSEE, H atoms bond to O atoms at the diagonal positions (SLEE is the most energetically  
170 unfavorable SiH configuration).

171 The starting crystal structures for the hydration models were constructed from the optimized  
172 anhydrous CaSiO<sub>3</sub> perovskite model. We removed Ca or Si atoms to create defects from the  
173 anhydrous structure and then added compensating H atoms at 1 Å away from the covalently  
174 bonded O atoms. The starting models of CaH assume that H atoms points to the center of the

175 dodecahedral site from the docking O atoms. In the SiH starting models, the H atoms point at  
176 adjacent O atoms in the octahedral sites. If H-unbonded O atoms are available in the octahedron,  
177 H atoms are aligned to point to those oxygen atoms.

178 The structures were calculated by relaxing all atomic positions (including H), cell shape, and  
179 unit-cell volume. We conducted calculations for the same computational conditions employed in  
180 the anhydrous model above (Tab. 1). While initially distinct, some models become identical to  
181 each other after optimization, such as CaH-SS' and CaH-LL', and CaH-SS and CaH-LL, as noted  
182 in the table. Also, we found that SiH-SLL structure becomes SiH-SSLE at 20 GPa. For the  
183 purpose of understanding the impact of higher concentration of H defects in CaH configurations,  
184 we conducted calculations for CaH-EE2 and CaH-SL'3, which are CaH-EE2×2 and CaH-SL'3×2,  
185 respectively.

186 The pressure-volume data we obtained from the DFT calculations were fit to Vinet equation  
187 (Vinet et al., 1989) for the effects of H<sub>2</sub>O substitution on the compressibility of CaSiO<sub>3</sub>  
188 perovskite. In order to simplify the comparison, we first conducted fitting for bulk modulus ( $K_0$ )  
189 only, while we fix unit-cell volume at 1 bar ( $V_0$ ) to the calculated values and pressure derivative  
190 of  $K_0$  ( $K'_0$ ) to 4.45 which is obtained for the anhydrous case (Tab. 2). We also conducted fitting  
191 for both  $K_0$  and  $K'_0$ . The fitting was conducted using the Pytheos package (Shim, 2017). The  $K_0$   
192 and  $K'_0$  we obtained for anhydrous CaSiO<sub>3</sub> perovskite are in agreement with previous studies  
193 (Chizmeshya et al., 1996; Akber-Knutson et al., 2002; Magyari-Köpe et al., 2002; Jung and  
194 Oganov, 2005; Kawai and Tsuchiya, 2015; Noguchi et al., 2013; Chen et al., 2018).

## 195 **Calculation of infrared spectra**

196 The infrared intensities were obtained by first re-optimizing the desired structural model to a  
197 high degree of convergence (residual cell stress and atomic forces less than 0.01 kbar and 0.0001  
198 eV/Å, respectively), and then calculating the  $\Gamma$ -point phonon frequencies and corresponding  
199 displacement vectors using density functional perturbation theory as implemented in the VASP  
200 code. In this part of the procedure, the dielectric response and Born effective charge tensor are  
201 systematically obtained (using the LEPSILON flag), then combined with the  $\Gamma$ -point phonon  
202 eigenvectors to obtain the infrared intensity of each mode (Porezag and Pederson, 1996). The  
203 resulting discrete spectra were then convoluted with a Gaussian function (width of 50 cm<sup>-1</sup>).

204

## 205 **Results and Discussions**

### 206 **Energetics of the hydrogen substitutions in CaSiO<sub>3</sub> perovskite**

207 As shown in Tab. 1 and Fig. 3, the energy difference between CaH models are smaller than ~0.5  
208 meV per atom for the pressure range we considered. This energy difference corresponds to 12 K  
209 and therefore that all the configurations we consider here are plausible for the H substitution  
210 mechanism and multiples of different H configurations considered here may exist together at  
211 mantle pressures and temperatures.

212 Among the models we studied, the CaH-EE2 model is similar to the arrangement of H atoms  
213 proposed for natural hydrous CaTiO<sub>3</sub> perovskite by Beran et al. (1996). The energy for the  
214 structure was the highest among the model we studied at 0 GPa. With compression, the structure  
215 becomes relatively more stable than other structures we considered. Although details were not  
216 provided, a stable H configuration in the dodecahedral site reported for bridgmanite in  
217 Hernández et al. (2013) appears to be similar to CaH-SS' which is the most stable H  
218 configuration at 0 GPa in our study (Fig. 3a).

219 SiH-SSEE has somewhat higher energy than SiH-SSLE, while the energy difference between the  
220 SiH-SSLE and SiH-SSEE models decreases with compression (Fig. 3b). H configurations similar  
221 to SiH-SSEE was documented as the lowest energy one alongside with SiH-SSLL (which  
222 transforms to SiH-SSLE at 20 GPa for CaSiO<sub>3</sub> perovskite) for bridgmanite in Hernández et al.  
223 (2013). SiH- SSEE is similar to the H configuration proposed for H in hydrous stishovite by  
224 Spektor et al. (2011). In this configuration, four out of six O atoms in an SiO<sub>6</sub> octahedron are  
225 bonded to H atoms and the other two remain unbonded to H. The four H atoms point at H-  
226 unbonded O atoms and they form a tetrahedron (the dotted lines in Fig. 2d). In SiH-SSEE, the  
227 centroids of the 4H polyhedron and the 6O octahedron match well. However, they are about 0.2  
228 Å off from each other in Si-SSLE. The most notable difference between these two structures is  
229 that the average H–H distance is greater in SiH-SSLE at lower pressures compared with SiH-  
230 SSEE (Fig. 4). This can be seen in the histograms in Fig. 5 which also show a much broader  
231 range of H–H distances in SSLE than SSEE. Among the broad range, SSLE shows very long H–

232 H distances at lower pressures, which may explain the slightly lower energy of the structure at  
233 lower pressures. The observation suggests that the smaller H–H distance and therefore stronger  
234 repulsion between them could make the SSEE configuration less stable than SSLE at lower  
235 pressures in CaSiO<sub>3</sub> perovskite.

236 It appears that H–H distance may not be the sole factor to decide the stability of H configurations  
237 in the CaH models as it is clear through comparison between Figs 3a and 5. In addition, while the  
238 average H–H distance becomes larger in SSEE than SSLE in SiH models at 50 GPa, SSLE still  
239 remains to be lower energy configuration up to 120 GPa, suggesting that there are other factors,  
240 such as tilting of the octahedra to accommodate the distortion around the defect sites.

### 241 **Unit-cell parameters and compressibility**

242 Chen et al. (2020) found that hydrous CaSiO<sub>3</sub> perovskite has a smaller unit-cell volume than  
243 anhydrous CaSiO<sub>3</sub> perovskite. They also showed that the peak splitting of the 200 line (the  
244 Miller index is for a pseudo-cubic cell) persists to mantle-related temperatures, suggesting the  
245 stabilization of a tetragonal structure at the conditions in the hydrous case. This observation is in  
246 sharp contrast with anhydrous CaSiO<sub>3</sub> perovskite where stability of a cubic structure has been  
247 found at mantle related temperatures and high pressures (Kurashina et al., 2004b; Chen et al.,  
248 2018).

249 Our results show that the unit-cell volume of hydrous CaSiO<sub>3</sub> perovskite does not change more  
250 than 0.07% from that of anhydrous CaSiO<sub>3</sub> perovskite at 1 bar for CaH (Fig. 6a). In the case of  
251 SiH, we found much larger volume expansion by hydration, more than 1.5%. Previous studies  
252 have found that the octahedral site substitution can significantly increase the unit-cell volume of  
253 hydrous stishovite (Spektor et al., 2011, 2016; Nisr et al., 2017, 2020). However, the SiH models  
254 have twice as much H as the CaH models. We also calculated CaH with two Ca defects for the H  
255 substitution, CaH-EE2×2 and CaHx2-SL'3×2. They both show increases in volume up to 5% at  
256 1 bar, suggesting that more hydration might possibly increase the volume for CaH at 0 GPa.

257 The unit-cell volume of hydrous CaSiO<sub>3</sub> perovskite becomes smaller than anhydrous case at  
258 pressures above 20 GPa for the CaH models (Fig. 6a). The CaH-EE2×2 and CaH-SL'3×2  
259 models suggest that more hydration would decrease the volume at high pressure even further.  
260 Because the SiH models decrease the bulk modulus, the unit-cell volumes of hydrous CaSiO<sub>3</sub>

261 perovskite from the SiH models become similar to the anhydrous CaSiO<sub>3</sub> perovskite with an  
262 increase in pressure. Both Fig. 6a and equation of state fit we presented in Tab. 2 show that H  
263 substitution makes CaSiO<sub>3</sub> perovskite more compressible.

264 From the smaller unit-cell volume of hydrous CaSiO<sub>3</sub> perovskite observed at high pressure and  
265 300 K, Chen et al. (2020) inferred that the dodecahedral site substitution is more likely than the  
266 octahedral site (SiH) substitution, because the dodecahedral site (CaH) substitution involves with  
267 removal of much larger sized Ca<sup>2+</sup>. Our DFT calculations found that the dodecahedral site  
268 substitution (the CaH models) can result in a smaller unit-cell volume of hydrous CaSiO<sub>3</sub>  
269 perovskite at mantle-related pressures, in qualitative agreement with the experimental  
270 observation. The experiments found approximately up to 1% reduction in the unit-cell volume at  
271 pressures between 2 and 45 GPa. At the similar pressure range we found 0 to 0.5% decrease in  
272 unit-cell volume for 1–2 wt% H<sub>2</sub>O in the CaH models. Chen et al. (2020) estimated 0.5–1 wt%  
273 H<sub>2</sub>O for their samples. Therefore, both studies are in general agreement in the magnitude of the  
274 changes in unit-cell volume for hydration level of a few percent.

275 Fig. 6b compares the *c/a* axial ratio of hydrous CaSiO<sub>3</sub> perovskite with anhydrous case. We  
276 found a little difference between the *a* and *b* axes, suggesting that tetragonal description for the  
277 unit-cell dimension is acceptable. At 300 K, Chen et al. (2018) reported 1.005 for the *c/a* ratio in  
278 anhydrous CaSiO<sub>3</sub> perovskite. Our DFT calculation suggests 1.02 for anhydrous case at 0 K  
279 without zero-point motion. Considering the fact that anhydrous CaSiO<sub>3</sub> perovskite transforms to  
280 a cubic structure at high temperature and the ratio therefore decreases with temperature, our DFT  
281 calculation is in reasonable agreement with the experimental report. Our *c/a* values agree well  
282 with those reported by Stixrude et al. (2007) through DFT calculation between 0 and 140 GPa at  
283 0 K, 1.013–1.020.

284 Chen et al. (2020) reported persistence of the 200 peak splitting, therefore *c/a* ≠ 1, in hydrous  
285 CaSiO<sub>3</sub> perovskite at mantle-related temperatures. The observation is in contrast with the known  
286 thermal behavior of anhydrous CaSiO<sub>3</sub> perovskite in that the peak splitting disappears, therefore  
287 *c/a* becomes 1, at temperatures greater than ~500 K (Kurashina et al., 2004a; Chen et al., 2018).

288 All the hydration models we studied show a significant deviation of *c/a* from 1. The SiH models  
289 show little difference from anhydrous case (Fig. 6b). The CaH-SS', CaH-EE2, and CaH-SS  
290 models in general increase the *c/a* ratio similar to the anhydrous case but the magnitude of the

291 deviation from  $c/a = 1$  is smaller. The CaH-SL'3, CaH-EE, and CaH-SE2 models show an  
292 opposite effect on the  $c/a$  ratio to the anhydrous case. From the comparison between CaH-EE2  
293 and CaH-EE2 $\times$ 2 models and between CaH-SL'3 and CaH-SL'3 $\times$ 2 models, it can be inferred that  
294 more H can increase the deviation of the  $c/a$  ratio from 1.

295 Thermal effects on the  $c/a$  ratio were not included in our calculations. So results do not directly  
296 address the question of whether the  $c/a$  ratio remains different from 1 or the peak splitting is still  
297 observable in diffraction patterns at mantle-related temperatures. However, the larger magnitude  
298 of distortion found particularly in 2 wt% H<sub>2</sub>O CaH cases may suggest that the peak splitting  
299 could remain observable at high temperature if the rate of decrease in the  $c/a$  ratio toward 1  
300 remains the same in those hydrous cases. However, fundamental reasons that hydrous CaSiO<sub>3</sub>  
301 perovskite can be non-cubic at high temperatures will be discussed in the next section.

### 302 **Bonding between hydrogen and oxygen atoms in hydrous CaSiO<sub>3</sub> perovskite**

303 The tetragonal distortion in the hydrous CaSiO<sub>3</sub> perovskite can be interpreted in two different  
304 ways: either by an ordered model that involves the ordering of the hydrogen-bearing defects, or a  
305 disordered model that results from a structural average of the defects occupied randomly. In this  
306 section, we discuss mostly for the former cases.

307 For the interpretation based on defect ordering, recent studies have suggested an important role  
308 of hydrogen bonding formation (O $\cdots$ H–O) and its potential symmetrization (O–H–O) for the  
309 crystal structure and physical properties of hydrous phases at high pressures and high tempera-  
310 tures, such as hydrous stishovite (Spektor et al., 2011; Nisr et al., 2017),  $\delta$ -AlOOH (Tsuchiya et  
311 al., 2002), and  $\epsilon$ -FeOOH (Gleason et al., 2013). It is believed that hydrogen bonding forms for a  
312 H-to-O distance less than  $\sim 2$  Å (Legon and Millen, 1987).

313 Fig. 7a shows histograms of the distances between neighboring O and H atoms in the studied  
314 hydration models for CaSiO<sub>3</sub> perovskite. For CaH-SS', CaH-SE2, CaH-SL'3, SiH-SSLE, and  
315 SiH- SSEE, we found increased population of the bond distances between 1 and 2 Å with  
316 compression. For example, in CaH-SS' at 120 GPa, an oxygen atom in the dodecahedral site  
317 approaches the second-neighbor H within 1.35 Å, while the O–H covalent bond stretches to 1.1  
318 Å. This behavior can be explained by enhanced hydrogen bonding (O $\cdots$ H) in these structures,  
319 leading to the increased population between 1 and 2 Å. As a consequence, the O–H covalent

320 bonding weakens, leading to an increase in the O–H distances. This behavior is more pronounced  
321 in the SiH models than the CaH models (reflected in more populations of the bonds between 1  
322 and 2 Å), likely because of the shorter distances among O atoms around the octahedral sites  
323 compared with those around the dodecahedral sites.

324 Fig. 7b shows histograms of the  $\angle\text{O–H}\cdots\text{O}$  angles within a distance (between O and H) of 2.0 Å.  
325 For the CaH-SS' and CaH-SL'3 configurations, the O–H $\cdots$ O bond angles remain between 140  
326 and 150° to the highest pressure, while CaH-SE2 develops the O–H $\cdots$ O bond angles between 80  
327 and 100° degrees particularly at pressures higher than 80 GPa. The CaH-SS' and CaH-SL'3  
328 configurations are the two lowest energy ones in the CaH group (Fig. 3). Therefore, structures  
329 which can facilitate the formation of stronger hydrogen bonding with more straight  $\angle\text{O–H}\cdots\text{O}$   
330 configuration can be energetically more advantageous. It is notable that CaH-SL'3 has shorter H–  
331 H distances (so more H–H repulsion) than CaH-SE2 at 120 GPa (Fig. 5). However, CaH-SL'3  
332 becomes the most stable configuration at the pressure (Fig. 3). Therefore, formation of nearly  
333 straight O–H $\cdots$ O bond may play an important role for the stabilization of H in CaSiO<sub>3</sub>  
334 perovskite.

335 In the SiH structures, larger population of shorter O $\cdots$ H bonds (or enhanced hydrogen bonding)  
336 form with O atoms at 80–120° (Fig. 7). Again, closer distances among O atoms around the  
337 octahedral sites are likely the reason. In the case of  $\delta\text{-AlOOH}$  and  $\epsilon\text{-FeOOH}$ , more straight O–  
338 H $\cdots$ O bonds have been suggested (Tsuchiya et al., 2002). The bond has been predicted to  
339 become symmetric with compression. In these structures, no octahedra are defective of cations  
340 and the H atoms bond with O atoms into tunnel like structures in CaCl<sub>2</sub> type structure. Our  
341 calculation shows that more deformed shapes of the defect polyhedra (the octahedron for SiH  
342 models and the dodecahedron for the CaH models) can facilitate O atoms to develop closer  
343 second neighbor distances with H and many of those O atoms exist at angles much lower than  
344 180°, although they tend to be less energetically favorable than near straight O–H $\cdots$ O bond.

345 The bonding between O and H atoms can induce some distortion in the crystal structure of  
346 CaSiO<sub>3</sub> perovskite. Fig. 8 shows the Si–O bond distances from the models in this study. The  
347 anhydrous (Anhy) structure has two groups of Si–O bond distances related to the tetragonal  
348 distortion of CaSiO<sub>3</sub> perovskite. Although the Si–O bond distances decrease with pressure, they  
349 maintain such grouping in the anhydrous case. Much more broad distribution of the Si–O

350 distances was found in hydrous  $\text{CaSiO}_3$  perovskite, while they maintain the same trend of overall  
351 population shifting to lower Si–O distances with pressure.

352 All CaH configurations show a small population of long Si–O bond distances persisting  
353 throughout the pressure range we studied as indicated by arrows for CaH-SL'3 as an example in  
354 Fig. 8. However, such a population does not exist in SiH. In SiH configurations, all O atoms  
355 have more similar interactions with H atoms in the defective site because of hydrogen bonding as  
356 discussed above and hence introduces less distortion to the Si–O bonding in the neighboring  
357 octahedra.

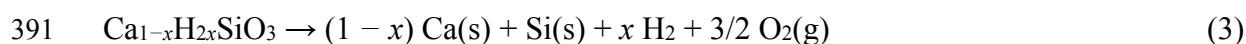
358 In the CaH models, these long Si–O distances are from the O atoms that are also bonded to H  
359 atoms (Si–O–H; see Fig. 2a,b). This type of O atoms also exists in the SiH models, but the main  
360 difference is that hydrogen bonding occurs to much less of a degree in CaH than in SiH.  
361 Therefore, the H atom in CaH weakens the covalent Si–O bonding much more than SiH, and the  
362 effect is more preferential for particular O atoms. Consequently, in CaH, the  $\text{SiO}_6$  octahedra are  
363 much more distorted from their ideal shapes than those in SiH. Such distorted  $\text{SiO}_6$  octahedra in  
364 the CaH configurations would make hydrous  $\text{CaSiO}_3$  perovskite intrinsically non-cubic. This  
365 situation would not change with heating as long as OH remains within the structure. This is in  
366 contrast to anhydrous case where the tetragonal distortion is mainly from the slight misfit of Ca  
367 in the dodecahedral sites at lower temperatures, which ultimately disappears by thermal vibration  
368 with heating. Therefore, the experimentally observed persistence of non-cubic peak splitting in  
369 diffraction patterns of hydrous  $\text{CaSiO}_3$  perovskite can be explained by the intrinsic structural  
370 distortion by H substitution (in particular CaH configurations).

371 Alternatively, if the symmetry-equivalent H-bearing defects of equal energy are fully disordered,  
372 then the tetragonal distortion of the perovskite can be due to a change in the apparent average  
373 cation sizes in the perovskite. We have noted that the apparent size of Si increases with the  
374 substitution of 4H onto Si vacancies, while the apparent size of Ca decreases with the  
375 substitution of 2H. Interestingly, if the hydrogen configurations on each defect are randomly  
376 distributed in the symmetry-equivalent configurations, the apparent octahedral size changes are  
377 isotropic on the scale of the macroscopic crystal sample. This means that the octahedral groups  
378 can remain nearly ideal (on average), and the result is that both types of substitution (CaH and  
379 SiH) will decrease the tolerance factor of the perovskite, defined as the bond length ratio (Ca–

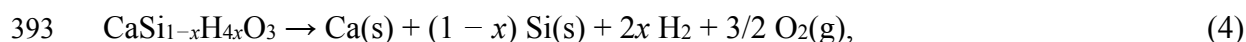
380 O)/( $\sqrt{2} \times (\text{Si-O})$ ). This has the well-known effect of driving the cubic perovskite (tolerance factor  
381  $\sim 1$ ) toward a tetragonal rotational subgroup (tolerance factor  $\sim 0.95$ ) similar to the example that is  
382 indicated by our data. Our current data cannot distinguish between the disordered possibility  
383 described here, or the ordered possibilities described above – high-quality crystallographic data  
384 on single crystals in the diamond-anvil cell will be required to distinguish between these  
385 possibilities.

## 386 **Energy difference between dodecahedral and octahedral hydrogen** 387 **substitutions**

388 The relative stability of  $\text{CaSiO}_3$  perovskite with the CaH and SiH configurations is determined  
389 by their Gibbs energy of formation relative to standard reference states  $\text{O}_2(\text{g})$ ,  $\text{Si}(\text{s})$ ,  $\text{H}_2(\text{g})$  and  
390  $\text{Ca}(\text{s})$ :



392 and



394 respectively. As a first order approximation, we estimate of the relative formation energies by  
395 calculating the ground state of the elemental reference states using the same numerical  
396 procedures and PAW-GGA pseudopotentials as in the CaH and SiH models. The diatomic  
397 molecules were treated by placing each species in a fixed but slightly distorted cubic cell of  
398 dimension  $\sim 10 \text{ \AA}$  and optimizing the internal structural coordinates. This procedure yielded the  
399 bond lengths of  $1.229 \text{ \AA}$  and  $0.750 \text{ \AA}$  for (triplet)  $\text{O}_2(\text{g})$  and  $\text{H}_2(\text{g})$ , respectively. Calcium and  
400 silicon were optimized as face-centered cubic structure and diamond cubic structure yielding cell  
401 lengths of  $5.53 \text{ \AA}$  and  $5.44 \text{ \AA}$ , respectively. Repeating the Ca and Si calculations using  $2 \times 2 \times 2$   
402 supercells (cell dimensions  $\sim 10\text{-}11 \text{ \AA}$ ) led to a negligible change in their respective energies.  
403 Using only the electronic DFT (neglecting vibrational free energy corrections) of the lowest  
404 energy models (LL'-90 for CaH and SSLE for SiH) we obtain  $\Delta E(\text{CaH}) = -1368 \text{ kJ/mol}$  and  
405  $\Delta E(\text{SiH}) = -1351 \text{ kJ/mol}$ , a difference of approximately 1%. This result suggests that at ambient  
406 pressure the formation energies of the CaH and SiH hydrous phases are similar.

## 407 **Infrared-active OH vibrational modes**

408 Chen et al. (2020) reported OH vibration model in infrared (IR) spectra of hydrous CaSiO<sub>3</sub>  
409 perovskite. The phase was synthesized from a hydrous starting material in LHDAC at 19 GPa  
410 and 1700 K (Fig. 9c). The documented OH vibrational features were broad (a width of ~200  
411 cm<sup>-1</sup>) at high pressures between 5 and 19 GPa. At their lowest pressure, 0.65 GPa, the OH  
412 feature becomes broader (~300 cm<sup>-1</sup>) before it disappears at 1 bar where CaSiO<sub>3</sub> perovskite  
413 amorphizes.

414 We conducted calculations for a few selected models in Fig. 9a,b. Significant differences were  
415 found between CaH and SiH models: the OH spectra of CaH structures are much simpler with a  
416 peak near 3600 cm<sup>-1</sup> at 0 GPa, while the spectra of SiH consist of at least 2 peaks spread over a  
417 wide wavenumber range between 2800 and 3800 cm<sup>-1</sup>. The most likely reason for the difference  
418 is that: while the OH in the dodecahedral sites do not interact with one another because of the  
419 large H–H distances (Fig. 5), the OH in the octahedral site has much more complicated bonding  
420 environment and interaction with nearby H and O atoms (Figs 5 and 7).

421 For the comparison with experimentally reported spectra, we assume that the thermal effects are  
422 small between 0 K (for our computation) and 300 K (for the experiments). Our calculation found  
423 100–200 cm<sup>-1</sup> decrease in the wavenumbers of the OH modes during compression from 0 to 30  
424 GPa. Assuming a linear response of mode frequencies to pressure, we estimate a 20–40 cm<sup>-1</sup>  
425 decrease in the mode frequency between our calculation (0 GPa) and the OH IR spectra at 5.5  
426 GPa by Chen et al. (2020). Therefore, given the broad nature of the OH vibration observed in  
427 experiment, the compressional effect is small.

428 Our calculation shows that the energy differences between various substitutional configurations  
429 are small among the CaH models and among the SiH models at 0 K. In addition, energy  
430 differences between the CaH and SiH models are small. Therefore, it is likely that multiples of  
431 different configurations exist together at mantle-related conditions (Tab. 1 and Fig. 3).  
432 Combination of SiH-SLL and SiH-SLE could explain the majority of the intensities observed  
433 in the OH region from experiment. These two SiH configurations have lowest energies among  
434 the considered SiH configurations at lower pressures (Tab. 1). As discussed before, SiH-SLL  
435 becomes SiH-SLE at 20 GPa. The sample by Chen et al. (2020) was synthesized at 19 GPa in  
436 experiments and 1700 K. Thermal effects could affect the relative stabilities of these two  
437 configurations. Therefore, both SiH-SLL and SiH-SLE could exist together in the

438 experimentally synthesized sample.

439 The experimentally measured spectra show much smaller intensity at the frequency region  
440 expected for the OH vibration from the CaH configurations. However, our calculation shows  
441 much smaller absorbance of the OH modes from CaH compared with SiH (approximately a  
442 factor of 10). Therefore, it is feasible that CaH configurations exist in a significant fraction in the  
443 hydrous CaSiO<sub>3</sub> perovskite but the intrinsically smaller absorbance from the OH from CaH  
444 created reduced intensities compared with the SiH configurations.

445 Fu et al. (2019) reported IR active OH vibration from single crystal (Mg,Fe)(Al,Si)O<sub>3</sub>  
446 bridgmanite. They found two major modes at ~3220 and ~3470 cm<sup>-1</sup> (Fig. 9d). While the modes  
447 are broader, wavenumbers of these two modes are similar to those observed in CaSiO<sub>3</sub>  
448 perovskite at ~3250 and ~3500 cm<sup>-1</sup> (Chen et al., 2020). The similarity may support comparison  
449 of our calculation on CaSiO<sub>3</sub> perovskite with the experimentally observed OH spectra from  
450 bridgmanite. The reported vibrational mode frequencies from bridgmanite are particularly  
451 comparable to the two IR modes predicted for the SiH-SSLE configuration (Fig. 7b). Although it  
452 is uncertain if the peak at 3700 cm<sup>-1</sup> in bridgmanite is from the sample rather than noise, if the  
453 mode is indeed from the sample, it can be related to OH in the dodecahedral sites. While a  
454 greater number of configurations is possible for bridgmanite because of its lower symmetry, our  
455 approach here can be used for calculating the energetics of different OH configurations and their  
456 IR spectra in bridgmanite in future studies, which will be important for understanding  
457 experimental observations regarding H<sub>2</sub>O storage in bridgmanite (Murakami et al., 2002; Bolfan-  
458 Casanova et al., 2003; Litasov and Ohtani, 2003; Fu et al., 2019)

459

## 460 **Summary and Implications**

461 The main findings of our study can be summarized as below:

- 462 • We consider all the possible dodecahedral (Ca<sup>2+</sup> → 2H<sup>+</sup>; CaH models) and octahedral  
463 (Si<sup>2+</sup> → 4H<sup>+</sup>; SiH models) substitution configurations for hydrogen in a tetragonal  
464 perovskite lattice of CaSiO<sub>3</sub>. The energy differences among the H configurations in the  
465 CaH and the SiH models are sufficiently small that multiples of H configurations will

- 466 likely exist together at mantle-related pressures and temperatures.
- 467 • Although distortion in the lattice can play an important role to stabilize diverse H  
468 configurations, our calculations suggest that (1) H–H repulsion, (2) hydrogen bonding,  
469 (2) and O–H···O angle are important factors for the energetics of the H configurations.
  - 470 • The impact of the dodecahedral substitutions on the crystal structure is more consistent  
471 with the X-ray diffraction observations. All the CaH models predict unit-cell volume  
472 decrease by H substitution. The CaH configurations result in much weaker hydrogen  
473 bonding. Therefore, O–H covalent bonding remains relatively strong, which introduces  
474 severe distortion in the neighboring SiO<sub>6</sub> octahedra. Such enhanced distortion appears to  
475 be more consistent with persistence of non-cubic crystal structure of CaSiO<sub>3</sub> perovskite in  
476 hydrous environments at high temperatures found in experiments (Chen et al., 2020).
  - 477 • Although some uncertainty remains, the magnitude of distortion predicted by DFT  
478 calculations for ~1 wt% H<sub>2</sub>O in CaSiO<sub>3</sub> perovskite is consistent with the experimentally  
479 reported distortions in the crystal structure, suggesting a few weight percent level H<sub>2</sub>O  
480 storage capacity of CaSiO<sub>3</sub> perovskite.
  - 481 • The infrared-active OH vibrational modes documented in recent experiments on CaSiO<sub>3</sub>  
482 perovskite (and bridgmanite) are more consistent with the SiH configurations. The  
483 observed large widths of the mode can be explained by existence of multiples of H  
484 configurations in the experimentally synthesized hydrous CaSiO<sub>3</sub> perovskite.

485 The persistence of a non-cubic distortion to mantle temperatures in hydrous CaSiO<sub>3</sub> perovskite  
486 opens up an interesting possibility for seismic investigation of hydrous regions in the lower  
487 mantle. CaSiO<sub>3</sub> perovskite represents as much as 23 wt% in the subducting basaltic layer (Hirose  
488 et al., 2005). The non-cubic distortion in hydrous CaSiO<sub>3</sub> perovskite at mantle temperatures  
489 could result in high elastic anisotropy in the hydrous subducting regions and therefore may open  
490 up a possibility to detect such hydrated structures in seismology. In fact, some seismic studies  
491 have found anisotropy around the subduction zones in the lower mantle (Chen and Brudzinski,  
492 2003; Panning and Romanowicz, 2006; Foley and Long, 2011).

493 Astrophysical measurements have found that some stars are rich in Ca compared with the Sun  
494 (Hinkel and Unterborn, 2018). If terrestrial planets form in the star systems, they would contain

495 more CaSiO<sub>3</sub> perovskite in the mantle, potentially making the lower mantle an important region  
496 for H<sub>2</sub>O storage. We also showed that the equation of state of CaSiO<sub>3</sub> perovskite can be affected  
497 by hydration. Our equations of state (Tab. 2) can be useful to model the internal structures of  
498 such exoplanets combined with measured mass-radius relations.

499 In order to further develop a deeper understanding of water storage in the deep mantle, it would  
500 be important to explore thermal effects in *ab initio* calculations in future studies. The systematic  
501 search for a range of possible H configurations we conducted here can be extended to lower  
502 symmetric perovskite structured phases in the lower mantle, i.e., bridgmanite, which is important  
503 to further advance our knowledge on water storage in the most volumetric layer in the Earth's  
504 interior, lower mantle.

505

## 506 **Acknowledgments**

507 We thank two anonymous reviewers for the discussion. The work has been supported by the  
508 NASA (80NSSC18K0353) grant to S.-H.S., A.C. and K.L. It has been also supported by NSF  
509 (EAR-2019565) grant to S.-H.S. and K.L. The results reported herein benefit from collaborations  
510 and information exchange within NASA's Nexus for Exoplanet System Science (NExSS)  
511 research coordination network sponsored by NASA's Science Mission Directorate. The authors  
512 acknowledge Research Computing at Arizona State University for providing HPC resources that  
513 have contributed to the research results reported within this paper.

514

## 515 **References**

- 516 Akber-Knutson, S., Bukowinski, M. S. T., Matas, J., 2002. On the structure and compressibility  
517 of CaSiO<sub>3</sub> perovskite. *Geophys. Res. Lett.* 29 (3), 4-1.
- 518 Bell, D. R., Rossman, G. R., 1992. Water in Earth's mantle: the role of nominally anhydrous  
519 minerals. *Science* 255 (5050), 1391.
- 520 Beran, A., Libowitzky, E., Armbruster, T., 1996. A single-crystal infrared spectroscopic and x-  
521 ray-diffraction study of untwinned San Benito perovskite containing OH groups. *The Canadian*  
522 *Mineralogist* 34 (4), 803–809.
- 523 Blochl, P. E., 1994. Projector augmented-wave method. *Physical review B* 50 (24), 17953.
- 524 Bolfan-Casanova, N., 2005. Water in the Earth's mantle. *Mineralogical Magazine* 69 (3), 229–  
525 257.
- 526 Bolfan-Casanova, N., Keppler, H., Rubie, D. C., 2003. Water partitioning at 660 km depth and  
527 evidence for very low water solubility in magnesium silicate perovskite. *Geophysical Research*  
528 *Letters* 30 (17) 10.1029/2003GL017182.
- 529 Caracas, R., Wentzcovitch, R., Price, G. D., Brodholt, J., 2005. CaSiO<sub>3</sub> perovskite at lower  
530 mantle pressures. *Geophys. Res. Lett.* 32 (6), L06306.
- 531 Chen, H., Leinenweber, K., Prakapenka, V., Prescher, C., Meng, Y., Bechtel, H., Kunz, M.,  
532 Shim, S.-H., 2020. Possible H<sub>2</sub>O storage in the crystal structure of CaSiO<sub>3</sub> perovskite. *Physics of*  
533 *the Earth and Planetary Interiors* 299, 106412.
- 534 Chen, H., Shim, S.-H., Leinenweber, K., Prakapenka, V., Meng, Y., Prescher, C., 2018. Crystal  
535 structure of CaSiO<sub>3</sub> perovskite at 28–62 GPa and 300 K under quasi-hydrostatic stress  
536 conditions. *American Mineralogist: Journal of Earth and Planetary Materials* 103 (3), 462–468.
- 537 Chen, W.-P., Brudzinski, M. R., 2003. Seismic anisotropy in the mantle transition zone beneath  
538 Fiji-Tonga. *Geophysical Research Letters* 30 (13), 10.1029/2002GL016330.
- 539 Chizmeshya, A. V. G., Wolf, G. H., McMillan, P. F., 1996. First-principles calculation of the  
540 equation-of-state, stability, and polar optic modes of CaSiO<sub>3</sub> perovskite. *Geophys. Res. Lett.* 23

- 541 (20), 2725–2728.
- 542 Enkovaara, J. e., Rostgaard, C., Mortensen, J. J., Chen, J., Du-lak, M., Ferrighi, L., Gavnholt, J.,  
543 Glinsvad, C., Haikola, V., Hansen, H., et al., 2010. Electronic structure calculations with GPAW:  
544 a real-space implementation of the projector augmented-wave method. *Journal of Physics:*  
545 *Condensed Matter* 22 (25), 253202.
- 546 Foley, B. J., Long, M. D., 2011. Upper and mid-mantle anisotropy beneath the tonga slab. *Geo-*  
547 *physical Research Letters* 38 (2) 1545-1552.
- 548 Fu, S., Yang, J., Karato, S.-i., Vasiliev, A., Presniakov, M. Y., Gavriliuk, A. G., Ivanova, A. G.,  
549 Hauri, E. H., Okuchi, T., Purevjav, N., et al., 2019. Water concentration in single-crystal (Al,  
550 Fe)-bearing bridgmanite grown from the hydrous melt: Implications for dehydration melting at  
551 the topmost lower mantle. *Geophysical Research Letters* 46 (17-18), 10346–10357.
- 552 Glazer, A., 1972. The classification of tilted octahedra in perovskites. *Acta Crystallographica*  
553 *Section B: Structural Crystallography and Crystal Chemistry* 28 (11), 3384–3392.
- 554 Gleason, A., Quiroga, C., Suzuki, A., Pentcheva, R., Mao, W., 2013. Symmetrization driven spin  
555 transition in  $\epsilon$ -FeOOH at high pressure. *Earth and Planetary Science Letters* 379, 49–55.
- 556 Gréaux, S., Irifune, T., Higo, Y., Tange, Y., Arimoto, T., Liu, Z., Yamada, A., 2019. Sound  
557 velocity of CaSiO<sub>3</sub> perovskite suggests the presence of basaltic crust in the Earth’s lower mantle.  
558 *Nature* 565 (7738), 218–221.
- 559 Gréaux, S., Nishiyama, N., Kono, Y., Gautron, L., Ohfuji, H., Kunimoto, T., Menguy, N.,  
560 Irifune, T., 2011. Phase transformations of Ca<sub>3</sub>Al<sub>2</sub>Si<sub>3</sub>O<sub>12</sub> grossular garnet to the depths of the  
561 Earth’s mantle transition zone. *Physics of the Earth and Planetary Interiors* 185 (3-4), 89–99.
- 562 Grocholski, B., Catalli, K., Shim, S.-H., Prakapenka, V., 2012. Mineralogical effects on the  
563 detectability of the postperovskite boundary. *Proceedings of the National Academy of Sciences*  
564 109 (7), 2275–2279.
- 565 Hernández, E. R., Alfe, D., Brodholt, J., 2013. The incorporation of water into lower-mantle  
566 perovskites: A first-principles study. *Earth and Planetary Science Letters* 364, 37–43.
- 567 Hinkel, N. R., Unterborn, C. T., 2018. The star–planet connection. I. Using stellar composition to

- 568 observationally constrain planetary mineralogy for the 10 closest stars. The Astrophysical  
569 Journal 853 (1), 83.
- 570 Hirose, K., Takafuji, N., Sata, N., Ohishi, Y., 2005. Phase transition and density of subducted  
571 MORB crust in the lower mantle. Earth and Planetary Science Letters 237 (1), 239–251.
- 572 Hirschmann, M. M., 2006. Water, melting, and the deep earth H<sub>2</sub>O cycle. Annu. Rev. Earth  
573 Planet. Sci. 34, 629–653.
- 574 Jung, D. Y., Oganov, A. R., 2005. Ab initio study of the high-pressure behavior of CaSiO<sub>3</sub>  
575 perovskite. Phys. Chem. Miner. 32 (2), 146–153.
- 576 Kawai, K., Tsuchiya, T., 2015. Small shear modulus of cubic CaSiO<sub>3</sub> perovskite. Geophysical  
577 Research Letters 42 (8), 2718–2726.
- 578 Kesson, S. E., Fitz Gerald, J. D., Shelley, J. M., 1998. Mineralogy and dynamics of a pyrolite  
579 lower mantle. Nature 393 (6682), 252–255.
- 580 Kohlstedt, D., Keppler, H., Rubie, D., 1996. Solubility of water in the  $\alpha$ ,  $\beta$  and  $\gamma$  phases of  
581 (Mg,Fe)<sub>2</sub>SiO<sub>4</sub>. Contributions to Mineralogy and Petrology 123 (4), 345–357.
- 582 Kresse, G., Furthmüller, J., 1996. Efficient iterative schemes for ab initio total-energy  
583 calculations using a plane-wave basis set. Physical review B 54 (16), 11169.
- 584 Kurashina, T., Hirose, K., Ono, S., Sata, N., Ohishi, Y., 2004a. Phase transition in Al-bearing  
585 CaSiO<sub>3</sub> perovskite: implications for seismic discontinuities in the lower mantle. Physics of the  
586 Earth and Planetary Interiors 145 (1), 67–74.
- 587 Kurashina, T., Hirose, K., Ono, S., Sata, N., Ohishi, Y., 2004b. Phase transition in Al-bearing  
588 CaSiO<sub>3</sub> perovskite: implications for seismic discontinuities in the lower mantle. Phys. Earth  
589 Planet. Inter. 145 (1–4), 67–74.
- 590 Larsen, A. H., Mortensen, J. J., Blomqvist, J., Castelli, I. E., Christensen, R., Dulak, M., Friis, J.,  
591 Groves, M. N., Hammer, B., Hargus, C., et al., 2017. The atomic simulation environment—a  
592 python library for working with atoms. Journal of Physics: Condensed Matter 29 (27), 273002.
- 593 Lee, K. K., O'Neill, B., Panero, W. R., Shim, S.-H., Benedetti, L. R., Jeanloz, R., 2004.  
594 Equations of state of the high-pressure phases of a natural peridotite and implications for the

- 595 Earth's lower mantle. *Earth and Planetary Science Letters* 223 (3-4), 381–393.
- 596 Legon, A., Millen, D., 1987. Angular geometries and other properties of hydrogen-bonded  
597 dimers: A simple electrostatic interpretation of the success of the electron-pair model. *Chemical*  
598 *Society Reviews* 16, 467–498.
- 599 Litasov, K., Ohtani, E., 2003. Stability of various hydrous phases in CMAS pyrolite-H<sub>2</sub>O system  
600 up to 25 GPa. *Physics and Chemistry of Minerals* 30 (3), 147–156.
- 601 Litasov, K., Ohtani, E., Langenhorst, F., Yurimoto, H., Kubo, T., Kondo, T., 2003. Water  
602 solubility in Mg-perovskites and water storage capacity in the lower mantle. *Earth and Planetary*  
603 *Science Letters* 211 (1-2), 189–203.
- 604 Litasov, K. D., Kagi, H., Shatskiy, A., Ohtani, E., Lakshtanov, D. L., Bass, J. D., Ito, E., 2007.  
605 High hydrogen solubility in Al-rich stishovite and water transport in the lower mantle. *Earth and*  
606 *Planetary Science Letters* 262 (3), 620–634.
- 607 Magyari-Köpe, B., Vitos, L., Grimvall, G., Johansson, B., Kollar, J., 2002. Low-temperature  
608 crystal structure of CaSiO<sub>3</sub> perovskite: An ab initio total energy study. *Phys. Rev. B: Condens.*  
609 *Matter Mater. Phys.* 65 (19), 193107.
- 610 Monkhorst, H. J., Pack, J. D., 1976. Special points for Brillouin-zone integrations. *Physical*  
611 *review B* 13 (12), 5188.
- 612 Murakami, M., Hirose, K., Yurimoto, H., Nakashima, S., Takafuji, N., 2002. Water in Earth's  
613 lower mantle. *Science* 295 (5561), 1885–1887.
- 614 Navrotsky, A., 1999. A lesson from ceramics. *Science* 284 (5421), 1788–1789.
- 615 Németh, P., Leinenweber, K., Ohfuji, H., Groy, T., Domanik, K. J., Kovács, I. J., Kovács, J. S.,  
616 Buseck, P. R., 2017. Water-bearing, high-pressure Ca-silicates. *Earth and Planetary Science*  
617 *Letters* 469, 148–155.
- 618 Nestola, F., Korolev, N., Kopylova, M., Rotiroti, N., Pearson, D., Pamato, M., Alvaro, M.,  
619 Peruzzo, L., Gurney, J., Moore, A., et al., 2018. CaSiO<sub>3</sub> perovskite in diamond indicates the  
620 recycling of oceanic crust into the lower mantle. *Nature* 555 (7695), 237.
- 621 Nisr, C., Chen, H., Leinenweber, K., Chizmeshya, A., Prakapenka, V. B., Prescher, C., Tkachev,

- 622 S. N., Meng, Y., Liu, Z., Shim, S.-H., 2020. Large H<sub>2</sub>O solubility in dense silica and its  
623 implications for the interiors of water-rich planets. *Proceedings of the National Academy of*  
624 *Sciences* 117 (18), 9747–9754.
- 625 Nisr, C., Leinenweber, K., Prakapenka, V., Prescher, C., Tkachev, S., Shim, S.-H. D., 2017.  
626 Phase transition and equation of state of dense hydrous silica up to 63 GPa. *Journal of*  
627 *Geophysical Research: Solid Earth* 122 (9), 6972–6983.
- 628 Noguchi, M., Komabayashi, T., Hirose, K., Ohishi, Y., 2013. High-temperature compression  
629 exper- iments of CaSiO<sub>3</sub> perovskite to lowermost mantle conditions and its thermal equation of  
630 state. *Phys. Chem. Miner.* 40 (1), 81–91.
- 631 Ohtani, E., Amaike, Y., Kamada, S., Ohira, I., Mashino, I., 2016. Stability of hydrous minerals  
632 and water reservoirs in the deep earth interior. *Deep Earth: Physics and chemistry of the lower*  
633 *mantle and core. Geophysical Monograph* 217, 265–275.
- 634 Panero, W. R., Pigott, J. S., Reaman, D. M., Kabbes, J. E., Liu, Z., 2015. Dry (Mg,Fe)SiO<sub>3</sub>  
635 perovskite in the Earth’s lower mantle. *Journal of Geophysical Research: Solid Earth* 120 (2),  
636 894–908.
- 637 Panning, M., Romanowicz, B., 2006. A three-dimensional radially anisotropic model of shear  
638 velocity in the whole mantle. *Geophysical Journal International* 167 (1), 361–379.
- 639 Pawley, A. R., McMillan, P. F., Holloway, J. R., 1993. Hydrogen in stishovite, with implications  
640 for mantle water content. *Science* 261, 1024–1024.
- 641 Pearson, D., Brenker, F., Nestola, F., McNeill, J., Nasdala, L., Hutchison, M., Matveev, S.,  
642 Mather, K., Silversmit, G., Schmitz, S., et al., 2014. Hydrous mantle transition zone indicated by  
643 ringwoodite included within diamond. *Nature* 507 (7491), 221–224.
- 644 Perdew, J. P., Burke, K., Ernzerhof, M., 1996. Generalized gradient approximation made simple.  
645 *Physical Review Letters* 77 (18), 3865.
- 646 Porezag, D., Pederson, M. R., 1996. Infrared intensities and Raman-scattering activities within  
647 density-functional theory. *Physical Review B* 54 (11), 7830.
- 648 Ricolleau, A., Perrillat, J.-p., Fiquet, G., Daniel, I., Matas, J., Addad, A., Menguy, N., Cardon,

- 649 H., Mezouar, M., Guignot, N., 2010. Phase relations and equation of state of a natural MORB:  
650 Implications for the density profile of subducted oceanic crust in the Earth's lower mantle.  
651 Journal of Geophysical Research: Solid Earth 115 (B8) 10.1029/2009JB006709.
- 652 Shim, S.-H., 2017. PeakPo - A python software for X-ray diffraction analysis at high pressure  
653 and high temperature. Zenodo, 10.5281/zenodo.810200.
- 654 Smith, E. M., Shirey, S. B., Richardson, S. H., Nestola, F., Bullock, E. S., Wang, J., Wang, W.,  
655 2018. Blue boron-bearing diamonds from Earth's lower mantle. Nature 560 (7716), 84–87.
- 656 Smyth, J. R., 1994. A crystallographic model for hydrous wadsleyite ( $\beta$ -Mg<sub>2</sub>SiO<sub>4</sub>): An ocean in  
657 the Earth's interior? American Mineralogist 79, 021–1024.
- 658 Spektor, K., Nylen, J., Mathew, R., Edén, M., Stoyanov, E., Navrotsky, A., Leinenweber, K.,  
659 Häussermann, U., 2016. Formation of hydrous stishovite from coesite in high-pressure  
660 hydrothermal environments. American Mineralogist 101 (11), 2514–2524.
- 661 Spektor, K., Nylen, J., Stoyanov, E., Navrotsky, A., Hervig, R. L., Leinenweber, K., Holland, G.  
662 P., Häussermann, U., 2011. Ultrahydrous stishovite from high-pressure hydrothermal treatment  
663 of SiO<sub>2</sub>. Proceedings of the National Academy of Sciences 108 (52), 20918–20922.
- 664 Stixrude, L., Lithgow-Bertelloni, C., Kiefer, B., Fumagalli, P., 2007. Phase stability and shear  
665 softening in CaSiO<sub>3</sub> perovskite at high pressure. Phys. Rev. B: Condens. Matter Mater. Phys. 75  
666 (2), 024108.
- 667 Thomson, A., Crichton, W., Brodholt, J., Wood, I., Siersch, N., Muir, J., Dobson, D., Hunt, S.,  
668 2019. Seismic velocities of CaSiO<sub>3</sub> perovskite can explain LLSVPs in Earth's lower mantle.  
669 Nature 572 (7771), 643–647.
- 670 Tsuchiya, J., Tsuchiya, T., Tsuneyuki, S., Yamanaka, T., 2002. First principles calculation of a  
671 high-pressure hydrous phase,  $\delta$ -AlOOH. Geophysical Research Letters 29 (19), 15-1.
- 672 Vinet, P., Rose, J. H., Ferrante, J., Smith, J. R., 1989. Universal features of the equation of state  
673 of solids. Journal of Physics: Condensed Matter 1 (11), 1941.
- 674

675 Figure 1: The dodecahedral arrangement of O atoms around a Ca atom (not shown for clarity)  
676 and the octahedral arrangement of O atoms around a Si atom (not shown for clarity) in CaSiO<sub>3</sub>  
677 perovskite for the consideration of H docking sites. The O atoms with the “S”, “E”, and “L”  
678 labels are for the atoms at shorter (red), intermediate (gray; at equatorial plane of the  
679 dodecahedron), and longer (blue) distances. For a Si vacancy, “S” and “L” are identical to each  
680 other because those O atoms are coordinated with neighboring Ca atoms at both short and long  
681 distances.

682  
683 Figure 2: Crystal structure of hydrous CaSiO<sub>3</sub> perovskite obtained from calculation results at 100  
684 GPa: **(a)** and **(b)** the dodecahedral site hydration models (equation 1), and **(c)** and **(d)** the  
685 octahedral site hydration models (equation 2). More information on the hydrogen substitution  
686 models can be found in Tab. 1. The light gray and the dark gray spheres are Si and O atoms,  
687 respectively. The red spheres are H atoms. In (c) and (d), the yellow octahedron at the center is  
688 the Si defect site for hydration. In those diagrams, the dashed lines connect four H atoms which  
689 forms a tetrahedral shape. The numbers are the Si–O bond distances in Å.

690  
691 Figure 3: Energies of **(a)** CaH models with respect to CaH-SS'. **(b)** SiH models with respect to  
692 SiH-SSLE at high pressures.

693  
694 Figure 4: The average H–H distances in the SiH models at high pressures.

695  
696 Figure 5: The H–H distances in the models we studied. The colors of the bars change from blue  
697 to red with an increase in pressure.

698  
699 Figure 6: Fractional differences in unit-cell volume between hydrous and anhydrous CaSiO<sub>3</sub>  
700 perovskite, **(a)** CaH and **(b)** SiH models. The *b/a* ratio for **(c)** CaH and **(d)** SiH models. The *c/a*  
701 ratio for **(e)** CaH and **(f)** SiH models.

702

703 Figure 7: (a) Distances between O and H atoms and (b) angles between O–H···O in the hydration  
704 models we studied at a range of pressures up to 120 GPa. The colors of the bars change from  
705 blue to red with an increase in pressure. Note that no O···H bond exists in (O–H distances shorter  
706 than 2 Å) in CaH-SS, CaH-EE, and CaH-EE2 structures throughout the pressure range we  
707 investigated.

708

709 Figure 8: The Si–O distances in the first neighbor. The colors of the bars change from blue to red  
710 with pressure. The arrows highlight a small but significant of population with very long Si–O  
711 distances. Such a population can be found in all CaH structures, while it is absent in the SiH  
712 structures.

713

714 Figure 9: Infrared spectra (IR) calculated for OH in (a) the dodecahedral sites (CaH) and (b) the  
715 octahedral sites (SiH) in CaSiO<sub>3</sub> perovskite. We also presented experimentally measured IR  
716 active OH modes of (c) CaSiO<sub>3</sub> perovskite from Chen et al. (2020) and (d) (Mg,Fe)(Al,Si)<sub>3</sub>  
717 perovskite (bridgmanite) from Fu et al. (2019).

718 Table 1: Energy calculated for variety of H substitution configurations at 0 GPa and static  
719 conditions. The CaH and SiH models are for the dodecahedral (a total of 81 atoms in the cell)  
720 and the octahedral (a total of 83 atoms in the cell) substitution configurations, respectively. S,  
721 E, and L represent oxygen atoms at shorter distances, intermediate distances, and longer  
722 distance from the dodecahedral center, respectively. ' is to note for an O atom at different  $z$   
723 (such as S1 and S4 in Fig. 1). Numbers 2 and 3 after the O notations indicate second and third  
724 neighbors between the oxygen atoms. If a number is not provided there, it means those oxygen  
725 atoms are next neighbors. The models which become identical to each other after optimization  
726 are shown in parenthesis. \* indicates models used for high pressure calculations. Degen.:  
727 degeneracy for different H coordination. Static lattice energies (e.g., neglecting zero-point  
728 energy) are listed relative to the lowest energy structure (denoted as  $\Delta E = 0$ ) in the “CaH” and  
729 “SiH” models, respectively.

Model	Degeneracy	$\Delta E$ (meV) <sup>730</sup>
CaH-SS' (or LL')*	4	0
CaH-SE2 (or LE2)*	8	6
CaH-SL'2	4	32 <sup>731</sup>
CaH-SS (or LL)*	2	33
CaH-EE*	4	86
CaH-SL'3*	4	220 <sup>732</sup>
CaH-EE2*	2	236
CaH-SL	8	377
CaH-SE	8	401
CaH-LE	8	405 <sup>733</sup>
SiH-SSLE (or LLSE)*	8	0
SiH-SLL*	1	190 <sup>734</sup>
SiH-SSEE (or LLEE)* SiH-SLEE	2 4	350 410

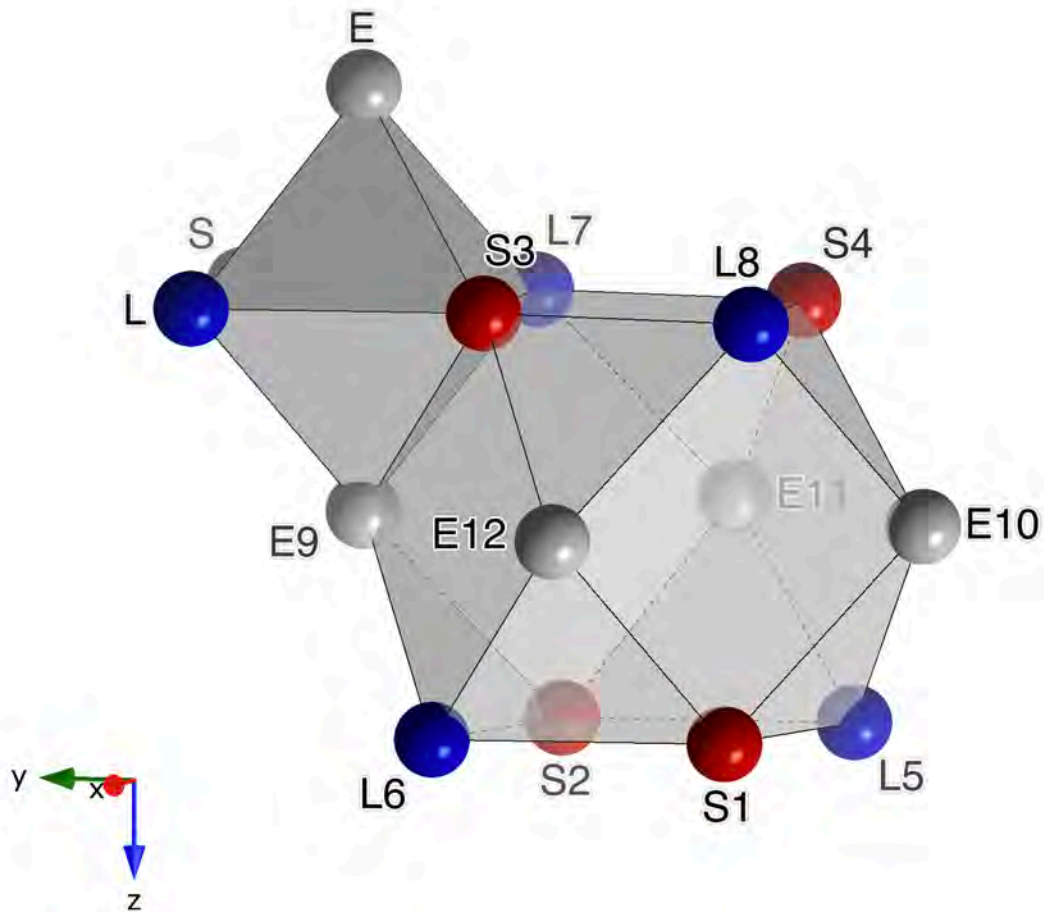
735

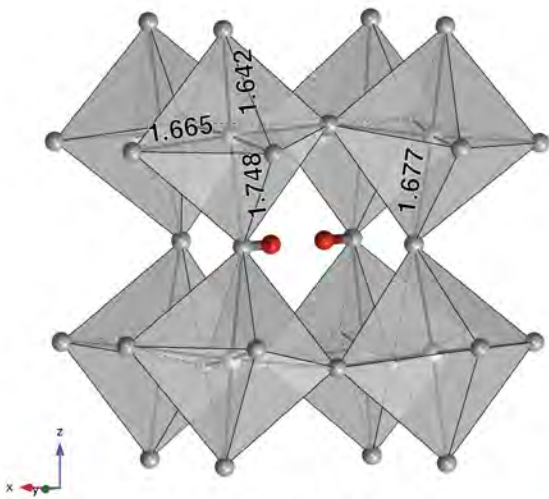
736

737 Table 2: Equation of state parameters for anhydrous and hydrous CaSiO<sub>3</sub> perovskite obtained  
738 from fitting to Vinet equation. We present two fitting results: (1) pressure-derivative of bulk  
739 modulus ( $K'_0$ ) fixed for  $K'_0 = 4.45$  ( $K_0^*$ ) and (2)  $K'_0$  varied. In the fitting, bulk modulus ( $K_0$ ) was  
740 varied while unit-cell volume at 1 bar ( $V_0$ ) was fixed. The  $K'_0 = 4.45$  results make the  
741 comparison among the models more straightforward, although the fitting strategy yielded higher  
742 estimated uncertainties (numbers in the parenthesis).

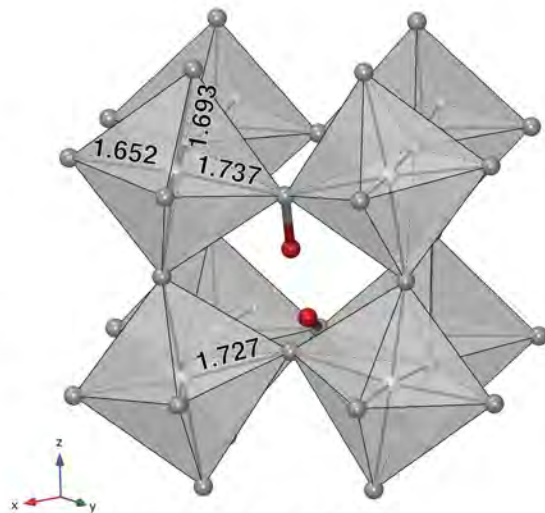
743

Model	$V_0$ (Å <sup>3</sup> )	$K_0^*$ (GPa)	$K_0$ (GPa)	$K'_0$
Anhy	47.392	211.72(4)	211.7(3)	4.45(1)
CaH-SS'	47.393	203.36(5)	202.9(3)	4.47(1)
CaH-SS	47.428	204.61(7)	205.5(1)	4.41(1)
CaH-SE2	47.389	203.26(6)	204.1(2)	4.42(1)
CaH-EE	47.424	203.52(11)	205.0(1)	4.39(1)
CaH-EE2	47.424	205.47(4)	205.0(1)	4.47(1)
CaH-SL'3	47.397	205.27(8)	204.2(4)	4.50(1)
SiH-SSLE	48.217	192.53(34)	187.8(2)	4.64(1)
SiH-SSEE	48.123	193.76(38)	188.5(2)	4.66(1)

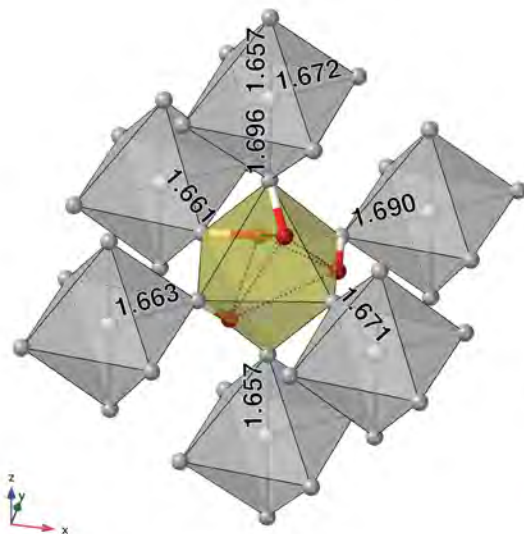




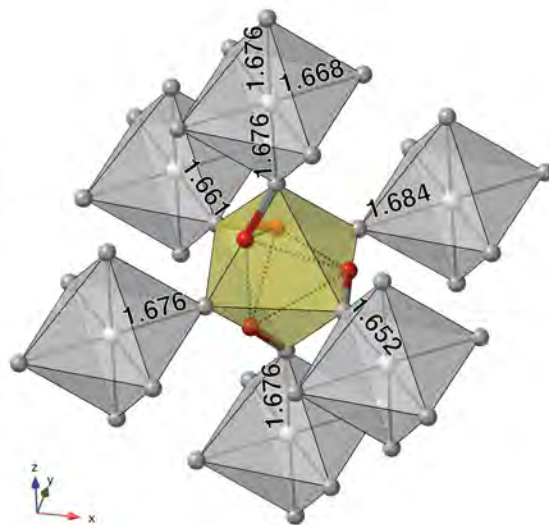
**(a) CaH-EE2**



**(b) CaH-SL'3**



**(c) SiH-SSLE**



**(d) SiH-SSEE**

